LLNL-JRNL-840448

LAWRENCE
LIVERMORE
NATIONAL
LABORATORY

Neon magnetron plasma deposition of boron carbide

S. J. Shin, L. B. Bayu Aji, J. H. Bae, A. M. Engwall, J. A. Hammons, G. V. Taylor, P. B. Mirkarimi, S. O. Kucheyev

September 28, 2022

Journal of Applied Physics

Magnetron sputter deposition of boron carbide in Ne and Ar plasmas

S. J. Shin,[1] L. B. Bayu Aji,[1] J. H. Bae,[2] A. M. Engwall,[1] J. A. Hammons,[1] G. V. Taylor,[1] L. R. Sohngen,[1] P. B. Mirkarimi,[1] and S. O. Kucheyev[1]

[1)]*Lawrence Livermore National Laboratory, Livermore, California 94550, U.S.A.*

[2)]*General Atomics, San Diego, California 92186, U.S.A.*

(*Electronic mail: Corresponding author. Tel: (925) 423-6707. E-mail: shin5@llnl.gov (S. J. Shin))

(Dated: 7 February 2024)

Conventional magnetron sputter deposition of B_4C uses Ar as the working gas. Here, we explore the magnetron sputter deposition of B_4C with a Ne plasma, which is expected to exhibit larger sputtering yields than Ar. We study properties of films deposited with different substrate tilt angles with the magnetron source operated in either direct-current (DC) or radio-frequency (RF) mode in an Ar or Ne plasma. Results show that B_4C film properties are determined by a combination of sputtering ballistics and effects of the working gas on the plasma discharge and gas phase scattering of depositing species flux. At constant discharge power, deposition rates for Ar and Ne plasmas are similar, which is attributed to balancing effects of a higher ballistic sputtering yield of Ne and lower ion flux to the target. Both depositing B and C neutral species and bombarding ions have higher energies for the case of Ne plasmas. Films deposited with the RF-driven Ne plasma exhibit a uniform non-columnar structure, lowest oxygen impurity content, and highest mass density and mechanical properties at a cost of Ne incorporation and larger compressive residual stress.

I. INTRODUCTION

Boron carbide, with typical stoichiometry of B_4C, possesses a unique combination of properties[1] of interest to several applications. These include light-weight armor,[2] nuclear reactor components,[3,4] and a diverse range of coatings for x-ray optics,[5–7] neutron detectors,[8,9] cutting and abrasive tools,[10,11] bearings,[12] shaving razor blades,[13] chemically-resistant components in semiconductor processing tools,[14] the first wall of tokamaks,[15] and hydrogen fuel ablator capsules for inertial confinement fusion (ICF).[16–25] This latter ICF-related application calls for ultrathick ($\sim 20-200$ μm) coatings with sub-micron-scale density uniformity. The deposition of such thick films is often limited by residual stress and process stability.[17]

Our recent systematic studies have identified deposition regimes for high-purity, low residual stress ($\lesssim 300$ MPa), amorphous B_4C films deposited by either direct-current or radio-frequency magnetron sputtering (DCMS or RFMS).[16,17,22–25] One of the remaining challenges is a relatively low deposition rate, which is related to a low sputtering yield of B_4C bombarded with Ar ions. Our recent experiments[16,17,22–25] and all the previous DCMS and RFMS studies of B_4C that we are aware of have been done with Ar as the working sputter gas. For relatively low ion energies typical for magnetron sources ($\sim 100-1000$ eV), the sputtering yield of B_4C bombarded with ^{40}Ar ions is expected to be low.[26–28] The sputtering yield may be increased by using lighter working gas ions such as ^{20}Ne that are better ballistically matched to light B and C atoms of the sputter target. In addition, a Ne plasma is expected to exhibit different energetics of landing ions and atoms during film growth, which could be used to control film properties. Here, we explore this by systematically studying properties of B_4C films deposited in the Ne plasma in either DCMS or RFMS mode and compare results with the case of films deposited with the conventional Ar plasma.

II. METHODS

A. Sputter deposition

Films were deposited by either DCMS or RFMS in a cylindrical high-vacuum chamber, 44 cm in diameter and 36 cm in height. The chamber walls and the substrate holder were maintained at ~ 30 °C with a base pressure of $\sim 5 \times 10^{-7}$ Torr prior to turning on the substrate heater. The base pressure increased to $\sim 1 \times 10^{-6}$ Torr when the substrate holder was heated to 450 °C prior to deposition. A substrate holder temperature of 450 °C was measured with an affixed thermocouple, and the corresponding substrate temperature, measured by imaging pyrometry (Optris GmbH, model PI 640),[24] was 330 °C.

The chamber was equipped with a 76.2-mm-diameter planar magnetron gun (the 3-inch MAK model from MeiVac Inc.) with a geometrical unbalance coefficient ~ 1.2 as used in our previous B_4C deposition studies.[16,17,22–25] Disk-shaped B_4C targets, supplied by Feldco International, had a diameter of 76.2 mm, an initial thickness of 6.4 mm, a density of 2.4 g cm^{-3}, and an electrical resistivity of 2×10^4 Ω cm. Targets were bonded with In to 76.2-mm-diameter, 3.2-mm-thick Cu backing plates. For the deposition runs described here, the total thickness of the target assembly (that includes an In metal bonding layer between the target and backing plate disks) at the racetrack center was in a narrow range of $\sim 7.9 - 8.6$ mm.

We used a custom-designed faceted substrate holder with substrate tilt angles of α = 0, 20, 40, 60, and 80 °, with $\alpha = 0°$ corresponding to the case when substrate and target surfaces are parallel. The holder was machined from a solid Mo block and was described in more detail previously.[23] Two types of substrates were mechanically clamped to each facet: (i) 10×10 mm^2 Si (100) chips with an $\sim$ 200-nm-thick Ta metal layer sputter deposited on top in a separate DCMS run and (ii) 3×12 mm^2, 262-μm-thick Si (100) cantilevers. The Ta layer on Si chips was used as a marker in areal density measurements by Rutherford backscattering spectrometry (RBS), while the cantilevers were used for residual stress measurements. All substrates were cleaned with ethanol and an air plasma exposure prior to deposition.

Sputter deposition conditions are summarized in Table I. The deposition was performed in the so-called sputter-down configuration with the electrically grounded substrate holder placed under the center of the B_4C target. Substrate temperature, the target-to-substrate distance, working gas pressure, and target power were selected based on results of our previous studies with Ar as the working gas.[22–25] The gas (99.998% purity for both Ar and Ne) flow rate was 25 standard cubic centimeters per minute, and RF power (300 W) was maintained with zero reflected power.

B. Film characterization

The B/C stoichiometric ratio and O, Ar, and Ne content in all films were measured by RBS with 2 MeV $^4He^+$ ions incident normal to the sample surface and backscattered into a detector located at 165° from the incident beam direction. The areal density was measured with either 2

MeV $^4He^+$ or $^1H^+$ ions in the same scattering geometry. The energy shift of the signal from the Ta marker layer was used to measure the areal density. The analysis of all RBS spectra was done with the RUMP code.[29]

Physical thickness of films was first measured by conventional stylus profilometry (KLA-Tencor, model D-100) and, to achieve higher accuracy, by cross-sectional scanning electron microscopy (SEM) in a Thermofisher Apreo instrument operated at 2 kV. Cross-sections for SEM measurements were prepared by mechanical fracture at room temperature propagating from the Si substrate side. Mass density was calculated by dividing the areal density measured with RBS by the physical thickness measured by SEM.

Residual stress was calculated with the Stoney equation based on the change in cantilever curvature measured by profilometry before and after deposition. The thermal stress component (σ_{TE}) originating from the difference in coefficients of thermal expansion between the film and the (Si) substrate was calculated with the following equation:

$$\sigma_{TE} = \frac{E_Y}{(1-\nu_f)}(\alpha_f - \alpha_s)\Delta T, \tag{1}$$

where ΔT is the difference between film growth and stress measurement temperatures, E_Y is the Young's modulus of the film (measured by nanoindentation as described below), ν_f is the Poisson's ratio of the film, and α_f and α_s are linear thermal expansion coefficients of the film and substrate, respectively. For the present study, $\Delta T = 310$ K, $\nu_f = 0.17$,[1], $\alpha_s = 3.6 \times 10^{-6}$ K^{-1},[30] and $\alpha_f = 4.6 \times 10^{-6}$ K^{-1},[24] respectively. Since σ_{TE} is tensile and relatively small (in the range of $\sim 50-150$ MPa, decreasing with increasing α due to the α dependence of E_Y), an average value of σ_{TE} of 100 MPa was used for plotting the data.

Mechanical properties were evaluated by nanoindentation in the load-controlled mode with an MTS XP nanoindenter with a Berkovich diamond tip. Meyer's hardness (H_M) was defined as average contact pressure, and E_Y was calculated based on the Oliver-Pharr method.[31] In Oliver-Pharr calculations, we assumed Poisson's ratios of diamond and B_4C films of 0.07 and 0.17, respectively, and a Young's modulus of diamond of 1141 GPa.[1,32] Measurements were performed over the indenter penetration depth range of $\sim 10-20\%$ of film thickness.

To resolve the in-plane nanoscale inhomogeneities in films, grazing incidence small-angle x-ray scattering (GISAXS) was employed. Films were studied with Cu-K$_\alpha$ x-rays in a Xeuss 3.0 instrument (Xenocs Inc.) under vacuum. Samples were secured to a holder such that the film surface plane was close to parallel to the x-ray beam propagation direction. The x-ray beam spot size was 0.7×0.2 mm^2 at tilt angles of $0.0 - 0.2^\circ$. Data was collected with a Pilatus3 300k detector in the "line-erasure" mode whereby two 2D patterns were obtained to remove the dead zones on the detector. In each case, a background scattering pattern was measured and found to be significantly below the scattering from the films. In order to compare the relative intensity scale, the intensity was normalized by taking into account slight differences in the x-ray beam path length for these samples. The reciprocal space unit vectors q_x, q_y, and q_z were chosen in such a way that the $q_x - q_y$ plane was parallel to the substrate, q_z was perpendicular to it, and q_x was perpendicular to the propagating x-ray beam. To a first approximation, the magnitude of the scattering vector, $|q|$, is inversely proportional to the physical dimensions of scattering centers (d) by the following relationship: $|q| \approx \frac{2\pi}{d}$. These GISAXS measurements were performed twice for each sample with sample-to-detector distances of 0.35 and 1.74 m to resolve small ($d \lesssim 5$ nm) and large ($d \sim 50$ nm) scattering features within the films, respectively.

C. Plasma diagnostics

Mass-resolved time-integrated energy distributions of B^+, C^+, Ar^+, and Ne^+ ions were measured for four representative conditions of this study (Table I) for a B_4C target (with a total thickness of ~ 9 mm) with the electrically grounded probe aperture located at a TSD of 100 mm on the axis of the magnetron source. The measurements were performed with an electrostatic quadrupole probe (Hiden Analytical, model EQP-6) with the front end magnetically shielded to 500 G.

D. Sputter yield measurements

Ballistic sputtering yield was evaluated based on measurements of the areal density of a sputter deposited amorphous B_4C film by RBS before and after irradiation with Ar ions generated by a broad beam ion source (KRI, model KDC 40).

E. Modeling

Monte Carlo modeling of gas phase transport of sputtered B and C atoms was performed with the SiMTra code[33] for our specific sputtering chamber and faceted substrate holder geometry described above. Trajectories of 10^8 atoms were tracked at room temperature separately for B and C, and values of landing energy (E) and the incident angle (θ) were recorded for each atom. Results for B and C atoms were stoichiometrically combined for each facet for an area of 2×2 cm^2. Sputtering yields as well as the initial energy and angular distributions of sputtered atoms, required for SiMTra, were calculated with the TRIM code[34] (version SRIM-2013.00) in the monolayer collision step mode. Ion energy was assumed to be equal to the target bias for each deposition run (Table I). The surface binding energy, lattice binding energy, and bulk displacement energy, for both B and C, were assumed to be 5.8, 3.0, and 20.0 eV, respectively, based on our sputter yield measurements described below.

III. RESULTS AND DISCUSSION

A. Plasma discharge characteristics

Figure 1(a) shows current–voltage ($I-V$) characteristics of the DCMS discharge (Ar and Ne), while Fig. 1(b) shows the taget self-bias voltage as a function of RF power for the RFMS discharge. It is seen from Fig. 1(b) that, for the RFMS discharge, the Ne plasma strikes at larger RF power and has larger self-bias voltage than for the Ar plasma. This is expected given a significantly larger (first) ionization potential of Ne than Ar (22 vs 16 eV).[35]

The difference between Ar and Ne discharge characteristics is much more striking for the DCMS case shown in Fig. 1(a). For Ar, the $I-V$ curve is a textbook example[36] of a superlinear magnetron discharge curve ($I_t \propto V_t^n$) with an exponent of $n \approx 6$. However, the $I-V$ curve for the Ne discharge is qualitatively different from that for Ar and from results in a report by Petrov et al.[37] The $I-V$ curve for Ne cannot be described by well-known empirical Thornton[38] and Westwood[39] equations. The Ne plasma strikes at a target voltage (V_t) of $\sim$ 345 V at a discharge power of $\sim$ 10 W, and V_t is actually slightly decreasing to 340 V with increasing discharge power to 300 W. More work is needed to understand the physics of Ne magnetron discharges and to establish how discharge characteristics depend on the magnetic field configuration and Ne pressure.

Such an essentially constant V_t at different discharge power levels for the Ne discharge [Fig. 1(a)] has a straightforward practical implication for future deposition rate studies which can be done via simply controlling the discharge power. This is in contrast to the conventional Ar discharge, for which deposition rate studies are complicated since changes to discharge power, working pressure, or the TSD (i.e., the experimental parameters that can be used to vary the deposition rate) influence discharge characteristics and, hence, landing atom and ion energetics.

B. Sputtering ballistics and gas phase transport

The choice of the working gas influences the plasma discharge characteristics, the sputter yield of the target, distributions of energies and angles of sputtered particles (neutrals), and gas phase scattering of sputtered atoms on their journey from the target to the substrate. Simulations provide valuable information about ballistic sputtering and gas phase scattering of neutrals.

We first discuss the sputter yield. Figure 2 summarizes TRIM code predictions of the dependence of the sputter yield of B_4C on ion energy for H and the noble gas species. Also shown in the plot by open star symbols are experimental data points for Ar ion bombardment. We used experimental Ar ion sputter yield data to benchmark predictions of TRIM code simulations as follows. In the input of TRIM code simulations, for both B and C atoms, lattice binding and bulk displacement energies were fixed to 3 and 20 eV, respectively, and the surface binding energy was adjusted to 5.8 eV until the experimental and predicted values of the sputter yield for 500 eV Ar ions matched. Figure 2 shows that, with these input parameters, TRIM predictions for the other three Ar energies of 600, 700, and 800 eV are in excellent agreement with experimental data.

Figure 2 further shows that the sputter yield monotonically increases with increasing ion energy for Ne and heavier ions, while the yield for H and He ions is essentially energy independent in the $200-800$ eV range studied here. Importantly, these TRIM simulations predict larger sputtering yields for lighter Ne ions than for heavier Ar ions in the entire ion energy range studied. Interestingly, for low energies of $\lesssim 400$ eV, He ions are predicted to have even larger sputter yields than Ne, and this prediction deserves future experimental verification.

Figure 3 shows key statistics of depositing species ballistics predicted by TRIM/SiMTra code simulations performed for the specific deposition chamber geometry and conditions for substrates mounted on the holder facets with different tilt angles α (which is the angle between the substrate normal and the magnetron sputter source axis). It is seen from Fig. 3 that α dependencies of the average landing energy $\overline{E}$ [Fig. 3(a)], average impact angle $\overline{\theta}$ [Fig. 3(c)], and their standard deviations ΔE and $\Delta\theta$ [Figs. 3(b) and 3(d)] for depositing B and C species have similar shapes for cases of Ar and Ne working gases for both RFMS and DCMS.

As we discussed in our previous study,[23] the weak $\overline{E}(\alpha)$ dependence for $\alpha \lesssim 60^\circ$ can be attributed to the fact that energy loss of light B or C atoms by collision with working gas atoms during their transport from the target to the substrate is small for these TSD and chamber pressure conditions. In this case, the initial energy distribution of B and C atoms sputtered from the target determines their landing energy distribution. While $\overline{\theta}(\alpha)$ and $\Delta\theta(\alpha)$ dependencies are essentially overlapping for all four cases, landing energy distributions are quantitatively different, with larger V_t corresponding to larger $\overline{E}$. The most energetic neutral flux is for the Ne-DC run, while Ar-RF run is characterized by the lowest landing atom energies. Hence, a Ne plasma offers more energetic deposition of atoms compared to the conventional Ar plasma.

C. Ion energy distributions

The Ne plasma also offers more energetic ion bombardment through the plasma sheath at the substrate. This is revealed by the mass-resolved ion energy distributions (IEDs) shown in Fig. 4 for the four representative conditions of this study. The three panels of Fig. 4 show distributions of B^+, C^+, and gas (Ar^+ or Ne^+) ions for the four deposition conditions of this study. Figure 4 reveals that IEDs depend strongly on the discharge mode (DCMS vs RFMS) and to a lesser extent on the working gas. For DCMS, Figs. 4(a) and 4(b) reveal expected unimodal IEDs for both Ar and Ne plasmas, with peaks centered on several electronvolts, corresponding to the plasma potential. In contrast, Figs. 4(c) and 4(d) show that the RFMS plasma is characterized by a significantly larger plasma potential compared to the case of DCMS. The IEDs for Ar-RF and Ne-RF cases exhibit the expected[40] saddle shape, with smaller saddle widths for heavier ions. The IEDs for Ar-RF and Ne-RF extend to ~ 50 and ~ 60 eV, respectively.

These findings of Monte Carlo simulations and plasma discharge diagnostics will be used to interpret experimental data below.

D. Deposition rate

Figures 5(a) and 5(b) show substrate tilt dependencies of the deposition rate based on measurements of the physical thickness and areal density of films, respectively. The deposition rate based on the physical thickness of the film [Fig. 5(a)] reflects the efficiency of target sputtering and atomic transport of sputtered atoms from the target to the substrate as well as the film microstructure and porosity. In contrast, the deposition rate based on the areal density [Fig. 5(b)], measured directly by RBS, is independent of the film microstructure and porosity. It is seen from Figs. 5(a) and 5(b) that, for all four runs, the deposition rate monotonically decreases with α. This is an expected trend since, with increasing substrate tilt and negligible gas phase scattering, the same atomic flux is being deposited onto a larger substrate area. Shown by open symbols in Fig. 5(b) are predictions of SiMTra/TRIM simulations that take into account gas phase scattering. These predictions describe well the experimental substrate tilt dependencies of the deposition rate.

Figures 5(a) and 5(b) further show that, for both Ar and Ne cases, the RFMS deposition rate is a factor of two lower than for DCMS. A lower deposition rate for RFMS than DCMS, with a constant discharge power, is in agreement with a number of previous observations, as we described in detail in our recent report.[25] Figure 5(b) further shows that, for RFMS, deposition rates for Ar and Ne plasmas are similar. For DCMS, the Ar plasma results in comparable or slightly higher deposition rates than Ne at different substrate tilt angles. This observation is somewhat unexpected and deserves a discussion, given a lower sputter yield for Ar than for Ne (Fig. 2) and a higher discharge voltage for Ar (Table I).

Comparable deposition rates in Ar-DC and Ne-DC runs could be attributed to the effect of a larger secondary electron emission coefficient of Ne than Ar. Indeed, for DCMS, the deposition rate (R) can be estimated as $R = A_{tran} Y_{sp} I_{ion}$, where Y_{sp} is the sputter yield, I_{ion} is ion current to the target, and A_{tran} is a parameter describing the angular dependence of sputtered particle flux and the efficiency of its transport from the target to the substrate. For DCMS, $I_{ion} = I_t/(1+\gamma_{SE})$, where I_t is the total target current and γ_{SE} is the average number of secondary electrons generated by each impinging ion. Hence, for deposition with discharge power W and target voltage V_t, the deposition rate is expected to scale as $R = \frac{A_{tran} Y_{sp} W}{V_t(1+\gamma_{SE})}$. With V_t from Table I, Y_{sp} from Fig. 2, γ_{SE} from Refs. 35 and 41, and A_{tran} from our SiMTra/TRIM simulations, the deposition rate for Ar and Ne plasma discharges is expected to be similar (with the Ar rate $\sim 14\%$ lower than Ne), which is in general agreement with experimental results of Fig. 5(b). In other words, the effect of a larger Y_{sp} for Ne ions is negated by their larger γ_{SE}.

E. Film density and its homogeneity

A further comparison of Figs. 5(a) and 5(b) reveals a significant difference between α dependencies of the deposition rates based on physical thickness [Fig. 5(a)] and areal density [Fig. 5(b)] measurements. This difference reflects changes in mass density, which is plotted in Fig. 5(c). Film density decreases with increasing α for all deposition conditions. This can be attributed to an increase in $\overline{\theta}$ [Fig. 3(a)] and the corresponding evolution of the columnar structure described below in Sec. III H. Films deposited with Ar as the working gas, in either DCMS or RFMS modes, have similar densities within measurement errors. In contrast, films deposited in Ne-DC and Ne-RF runs have measurably lower and higher densities, respectively, compared to the Ar-DC and Ar-RF runs.

Higher densities of films from the Ne-RF run can be attributed to a combination of the incorporation of Ne atoms into the film [Fig. 5(d), discussed below, and open symbols in Fig. 5(c)] and high ion energies of $35-60$ eV [Fig. 4(d)]. However, lower film densities for films from the Ne-DC run deposited at oblique angles of $\alpha \geq 40^\circ$ are puzzling since both $\overline{E}$ of depositing B and C atoms [Fig. 3(a)] and energies of ions [Figs. 4(a) and 4(b)] are slightly larger for the case for the Ne-DC than Ar-DC run. More energetic atoms are expected to increase adatom mobility, resulting in the growth of denser films. Lower density of Ne-DC films could be related to differences in energy transfer from Ar and Ne atoms and ions to the surface B and C atoms of the growing film in the regime when particle energies are lower than the threshold energies of atomic displacements in the bulk or surface sputtering. More work is needed to better understand the growth of B_4C films in such a subthreshold regime.

Information about density homogeneity is provided by GISAXS data in Fig. 6, showing a comparison of 2D scattering patterns for $\alpha = 0^\circ$ films deposited in Ne-DC [Fig. 6(a)] and Ne-RF [Fig. 6(b)] runs. Corresponding 1D in-plane scattering profiles for these films and $\alpha = 0^\circ$ films from Ar-DC and Ar-RF runs are given in Fig. 6(c), along with fitting the Yoneda region (i.e., the region of low q_x and q_z)[42] with a heuristic two-level unified equation, described in detail in our previous report.[25] A clear decrease in scattered intensity is observed for the Ne-RF film. Figure 6(d) shows the scaling parameter, ϕ_1, obtained from the invariant of the first level of the fitting equation.[25] This parameter ϕ_1 describes density heterogeneity. It is proportional to the concentration (volume fraction) of the scattering centers and the square of the difference in the electron density in the scattering sites and the matrix. Figure 6(d) reveals that the film from the Ne-RF run has the smallest density heterogeneity, while the film from the DC-Ne run exhibits the largest heterogeneity. A comparison of Figs. 5(c) and 6(d) shows that denser films have also better density homogeneity, which suggests that nanoscale film porosity is responsible for the density reduction in these films.

F. Impurity content

Working noble gas and oxygen atoms are the two most common unintentional impurities in sputter deposited films. Noble gas impurities originates from implanted working gas atoms (Ar and Ne in the present study), while O comes from water molecules, which are the most abundant residual gas molecules present in high-vacuum stainless steel chambers like the one used in the present study. For both DCMS and RFMS films deposited with the Ar plasma, Ar content is below the detection limit of our RBS measurements ($\lesssim 0.2$ at.%) and, hence, not plotted in Fig. 5(d). Low Ar content is consistent with results of our previous DCMS study of B_4C.[23]

On the other hand, Ne impurities are detected in films from both Ne-DC and Ne-RF runs, with Ne-RF films exhibiting a particularly high Ne concentration of ~ 7 at.% for $\alpha = 0°$ and $20°$ films for the Ne-RF run [Fig. 5(d)]. The incorporation of Ne can be attributed to implantation of Ne ions accelerated in the plasma sheath at the substrate. Indeed, Fig. 4(d) reveals that, for the Ne-RF run, Ne ions have energies in the range of $\sim 35-55$ eV. A further comparison of IEDs (Fig. 4) and working gas impurity content [Fig. 5(d)] suggests that, for similar ion energies, Ne incorporates into B_4C during growth much more efficiently compared to Ar.

Enhanced Ne retention cannot be explained by differences in the implantation depth of ^{40}Ar and ^{20}Ne ions. For example, TRIM code simulations show that, at 40 eV, the projected range of Ar and Ne ions in B_4C is essentially the same (~ 1 nm). Larger retention of Ne than Ar suggests higher effective diffusivity of Ar. It could be related to effects of ballistic atomic displacements, creating short-range order (bonding) defects, on noble gas atom diffusivity. Based on TRIM code simulations, at 40 eV, Ne ions are better ballistically matched than Ar to B and C atoms of the film and create twice as many atomic displacements per ion (2.95 vs 1.51 vacancies per ion). Moreover, with constant energy, compared to Ar ions, Ne ions are capable of transferring ~ 1.4 times larger maximum energy in collisions with B or C atoms since the maximum energy transferred in an elastic collision is $\frac{4m_1m_2E}{(m1+m2)^2}$, where E is the ion energy and m_1 and m_2 are particle masses. The difference in the maximum transferred energy will play a major role if diffusion involves processes with threshold energies related to various surface and bulk atomic bonding configurations. More work is clearly needed to better understand defect formation during B_4C film growth and its influence on impurity diffusivity and retention.

Figure 5(e) shows that O was detected in all the films. Oxygen content is relatively low in all the cases ($\lesssim 5$ at.%). It monotonically increases with α for all deposition conditions. The difference in

O content between the four runs is within experimental errors of these RBS measurements. The α dependence of O content suggests that columnar boundaries harbor O impurities. We will discuss this in Sec. III H below.

G. Residual stress

Figure 7(a) shows the α dependence of residual stress (σ) in films, revealing close-to-zero intrinsic stress for all films except for those deposited in Ne-RF run. The magnitude of compressive σ of ~ 5 GPa for the $\alpha = 0°$ film from the Ne-RF run is much larger than in any of our previous studies of B_4C.[16,17,22–25] These Ne-RF films have not delaminated since they were of sub-micron thickness (Table I).

The shape of the $\sigma(\alpha)$ dependence for the Ne-RF run is similar to that revealed in our recent studies[16,25] for B_4C films deposited with the Ar plasma at a lower pressure of 6 mTorr. Compressive σ is maximum for films deposited on untilted substrates ($\alpha = 0°$), and it decreases with increasing α. The $\sigma(\alpha)$ dependence can be attributed to a combination of ion energetics effects described above (larger Ne energies and a larger number of atomic displacements generated by Ne ions than by Ar ions with the same energy) and the lack of the columnar microstructure in Ne-RF films, as we describe below.

H. Microstructure

The microstructure of films from each of the four runs for α = 0 and 60° is illustrated in representative SEM micrographs in Figs. 8 and 9, respectively. In these figures, left columns are plan-view and right columns are corresponding fracture-cross-sectional micrographs. Both plan-view and cross-sectional SEM micrographs in Figs. 8 and 9 reveal a columnar structure for most of the films. The average column width is ~ 100 nm, independent of α. A notable exception is the $\alpha = 0°$ film from the Ne-RF run, whose SEM cross-section is shown in Fig. 8(d). The cross-section is featureless, revealing lack of the columnar structure. Cross-sectional SEM characterization of the $\alpha = 20°$ film from the Ne-RF run [SEM micrographs not shown but similar to those in Fig. 8(d)] also showed no columnar structure.

Cross-sectional SEM micrographs from right columns of Fig. 9 shows that films deposited on substrates tilted to 60° have a columnar structure with tilted columns. We have analyzed such cross-sectional SEM micrographs for all the films, and the dependence of the column tilt angle (β) on α is plotted in Fig. 7(b). An angle β of 0° corresponds to columns aligned with the film growth direction. Such a $\beta(\alpha)$ dependence has been studied extensively for other materials over many decades.[43–45] The two most frequently used correlations are the empirical cosine[46] and the tangent rules.[47] These are also plotted in Fig. 7(b) by solid and dashed lines, respectively. It is clear that these empirical rules cannot describe our experimental $\beta(\alpha)$ curves which are sublinear and much weaker than these empirical predictions.

Figure 7(b) further shows that films from the Ne-RF run exhibit much larger β values for α of 40, 60, and 80°; i.e., for cases with a columnar structure (as opposed to films deposited at $\alpha = 0$ and 20° with no columnar structure). This result is intriguing. It can be compared with results of our recent study[25] of the effect of Ar working gas pressure on properties of B_4C films deposited by RFMS, where we have found that films deposited at low pressures, characterized by depositing atoms with higher energies and lower average impact angles, do not exhibit a columnar structure. This suggests that the formation of a columnar structure is related to a reduced mobility of adatoms and larger atom impact angles. More work is currently needed to better understand the nucleation and growth of columnar B_4C films and roles of residual stress, impurities, ballistic displacements, and adatom diffusivity.

I. Mechanical properties

Mechanical properties (E_Y and H_M) measured by nanoindentation are presented in Figs. 7(c) and 7(d). Both E_Y and H_M monotonically decrease with increasing α. For $\alpha \geq 40°$, the Ne-RF films have largest E_Y and H_M, while Ne-DC films have the smallest. This behavior of E_Y and H_M can be correlated with changes in film density [Fig. 5(c)] and the columnar microstructure, with B-rich columns and O-rich inter-columnar regions.[23]. Interestingly, mechanical properties of the films from Ne-RF run show a very weak dependence on α.

IV. SUMMARY

In summary, we have reported a comparative study of properties of B_4C films deposited at different substrate tilt angles by either DCMS or RFMS with either Ar or Ne working gas under otherwise identical conditions (of Table I). Our main results can be summarized as follows.

- The energy dependence of the ballistic sputter yield of amorphous B_4C films under Ar ion irradiation has been measured (Fig. 2). Despite the known limitations[48] of the TRIM code[34] to predict sputtering with low-energy ions, the experimental sputter yield can be described by TRIM code simulations with the following input parameters: surface binding energy, lattice binding energy, and bulk displacement energy, for both B and C, of 5.8, 3, and 20 eV, respectively.

- For constant discharge power and the conditions of this study (Table I), deposition rates for Ar and Ne are comparable in either the DCMS or RFMS mode. This observation has been attributed to opposing effects of a larger sputter yield of Ne ions and their larger secondary electron coefficient compared to the case of the Ar discharge at constant discharge power. The deposition rate is ~ 2 times lower for RF than for DC, which can be attributed to corresponding differences in the partitioning of the discharge energy between processes of ion acceleration across the sheath (resulting in sputtering) and various ionization, heating, and radiation processes not contributing to sputtering.

- Films deposited with the Ne plasma in the RFMS mode exhibit the absence of the columnar structure, lower O impurity content, higher densities, and improved mechanical properties. Such improvements are accompanied by increased Ne atom incorporation and compressive residual stress.

- Without further studies, increased residual stress and Ne impurity content preclude the use of Ne plasmas for the fabrication of B_4C-based ICF ablators, which have strict limits on impurity concentrations. However, the favorable morphological, structural, and mechanical properties of B_4C films deposited by RFMS in Ne plasmas could be useful for other applications seeking to achieve the best mechanical properties, isotropic properties without a columnar structure, and/or highest film density.

ACKNOWLEDGMENTS

This work was performed under the auspices of the U.S. DOE by LLNL under Contract DE-AC52- 07NA27344 and by General Atomics under Contract 89233119CNA000063 and was supported by the LLNL-LDRD program under Projects No. 20-ERD-029.

REFERENCES

[1]F. Thevenot, “Boron carbide – A comprehensive review,” J. Europ. Ceram. Soc. **6**, 205 (1990).

[2]K. Y. Xie, K. Kuwelkar, R. A. Haber, J. C. LaSalvia, and K. J. Hemker, “Microstructural characterization of a commercial hot-pressed boron carbide armor plate," J. Am. Ceram. Soc. **99**, 2834 (2016).

[3]H. Guo, P. Sciora, T. Kooyman, L. Buiron, and G. Rimpault, “Application of boron carbide as burnable poison in sodium fast reactors,” Nucl. Technol. **205**, 1433 (2019).

[4]X. Li, J. Wu, C. Tang, Z. He, P. Yuan, Y. Sun, W. Lau, K. Zhang, J. Mei, and Y. Huang, “High temperature resistant polyimide/boron carbide composites for neutron radiation shielding,” Compos. Part B-Eng. **159**, 355 (2019).

[5]D. L. Windt, “Reduction of stress and roughness by reactive sputtering in W/B_4C X-ray multilayer films,” Proc. SPIE **6688**, R6880 (2007).

[6]R. Soufli, A. L. Aquila, F. Salmassi, M. Fernández-Perea, and E. M. Gullikson, “Optical constants of magnetron-sputtered boron carbide thin films from photoabsorption data in the range 30 to 700 eV,” Appl. Optics **47**, 4633 (2008).

[7]J. L. Wu, R. Z. Qi, Q. S. Huang, Y. F. Feng, Z. S. Wang, and Z. H. Xin, “Stress, roughness, and reflectivity properties of sputter-deposited B_4C coatings for x-ray mirrors,” Chin. Phys. Lett. **36**, 120701 (2019).

[8]C. Höglund, J. Birch, K. Andersen, T. Bigault, J. C. Buffet, J. Correa, P. van Esch, B. Guerard, R. Hall-Wilton, J. Jensen, A. Khaplanov, F. Piscitelli, C. Vettier, W. Vollenberg, and L. Hultman, “B_4C thin films for neutron detection,” J. Appl. Phys. **111**, 104908 (2012).

[9]Z. Zhang, Y. Liang, W. Li, Z. Wang, and H. Chen, “Stress evolution in B_4C and Cr mono-layer and B_4C/Cr multilayer with variable layer thickness for neutron detectors,” Thin Solid Films **531**, 302 (2013).

[10]E. Eichen, J. D. Flasck, Ovonic Synthetic Materials Co Inc, 1987. “Disordered coating.” U.S. Patent 4,716,083.

[11]O. Knotek, E. Lugscheider, and C. W. Siry, “Superhard PVD coatings in the B-C-N triangle,” Int. J. Refract. Met. H. **17**, 157 (1999).

[12]G. L. Doll, The Timken Company, 2003. “Bearing with amorphous boron carbide coating.” U.S. Patent 6,517,249 B1.

[13]R. F. Boland, C. A. Hultman, W. E. Vreeland, P. S. Williams, Warner-Lambert Company, 1992.

"Shaving razors." U.S. Patent 5,088,202.

[14]H. Shih, N. Han, S. S. Y. Mak, G. Z. Yin, Applied Materials Inc, 2000. "Boron carbide parts and coatings in a plasma reactor." U.S. Patent 6,120,640.

[15]O. I. Buzhinskij, and Y. M. Semenets, "Thick boron carbide coatings for protection of tokamak first wall and divertor," Fusion Eng. Des. **45**, 343 (1999).

[16]S. J. Shin, L. B. Bayu Aji, A. M. Engwall, J. H. Bae, G. V. Taylor, P. B. Mirkarimi, C. Aracne-Ruddle, J. Nguyen, C. W. N. Kong, and S. O. Kucheyev "Ultrathick boron carbide coatings for nuclear fusion", Fusion Sci. Technol. **79**, 841 (2023).

[17]S. O. Kucheyev, S. J. Shin, L. B. Bayu Aji, J. H. Bae, A. M. Engwall, and G. V. Taylor, "Development of new magnetron sputter deposition processes for laser target fabrication, " Fusion Sci. Technol. **79**, 823 (2023).

[18]T. R. Dittrich, S. W. Haan, S. Pollaine, A. K. Burnham, and G. L. Strobel, "NIF capsule design update," Fusion Sci. Technol. **31**, 402 (1997).

[19]A. K. Burnham, C. S. Alford, D. M. Makowiecki, T. R. Dittrich, R. J. Wallace, E. C. Honea, and C. M. King, "Evaluation of B4C as an Ablator Material for NIF Capsules," Fusion Sci. Technol. **31**, 456 (1997).

[20]A. S. Moore, S. Prisbrey, K. L. Baker, P. M. Celliers, J. Fry, T. R. Dittrich, K J. J. Wu, M. L. Kervin, M. E. Schoff, M. Farrell, A. Nikroo, and O. A. Hurricane, "A simulation-based and analytic analysis of the off-Hugoniot response of alternative inertial confinement fusion ablator materials," High Energ. Dens. Phys. **20**, 23 (2016).

[21]R. Chen, J. Qi, Q. Shi, X. Guo, D. Wu, T. Lu, and Z. Liao, "Rapid preparation and uniformity control of B_4C ceramic double-curvature shells: Aim to advance its applications as ICF capsules," J. Alloys and Compounds **762**, 67 (2018).

[22]A. M. Engwall, L. B. Bayu Aji, S. J. Shin, P. B. Mirkarimi, J. H. Bae, and S. O. Kucheyev, "Sputter-deposited low-stress boron carbide films," J. Appl. Phys. **128**, 175301 (2020).

[23]S. J. Shin, L. B. Bayu Aji, J. H. Bae, A. M. Engwall, M. H. Nielsen, J. A. Hammons, X. B. Zuo, B. Lee, X. Lepro, P. B. Mirkarimi, and S. O. Kucheyev, "Oblique angle deposition of boron carbide films by magnetron sputtering," J. Appl. Phys. **130**, 125305 (2021).

[24]L. B. Bayu Aji, S. J. Shin, J. H. Bae, A. M. Engwall, J. A. Hammons, X. Lepro, N. Catarineu, P. B. Mirkarimi, and S. O. Kucheyev, "Effect of substrate temperature on sputter-deposited boron carbide films," J. Appl. Phys. **131**, 075304 (2022).

[25]L. B. Bayu Aji, S. J. Shin, J. H. Bae, A. M. Engwall, J. A. Hammons, S. T. Sen-Britain, P. B.

Mirkarimi, and S. O. Kucheyev, “Radio-frequency magnetron sputter deposition of ultrathick boron carbide films,” J. Vac. Sci. Technol. A **41**, 023407 (2023).

[26]T. Ono, T. Kawamura, K. Ishii, and Y. Yamamura, “Sputtering yield formula for B_4C irradiated with monoenergetic ions at normal incidence,” J. Nucl. Mater. **232**, 52 (1996).

[27]E. Gauthier, W. Eckstein, J. Laszlo, and J. Roth, “Physical sputtering of low-Z materials,” J. Nucl. Mater. **176-177**, 438 (1990).

[28]E. Hechtl, A. Mazanec, W. Eckstein, J. Roth, and C. Garcia-Rosales, “Sputtering behavior of boron and boron carbide,” J. Nucl. Mater. **196**, 713 (1992).

[29]L. S. Doolittle, “Algorithms for the rapid simulation of Rutherford backscattering spectra,” Nucl. Instrum. Methods Phys. Res. B **9**, 344 (1985).

[30]H. Watanabe, N. Yamada, and M. Okaji, “Linear thermal expansion coefficient of silicon from 293 to 1000 K,” Int. J. Thermophys. **25**, 221 (2004).

[31]W. C. Oliver and G. M. Pharr, “An improved technique for determining hardness and elastic modulus using load and displacement sensing indentation experiments,” J. Mater. Res. **7**, 1564 (1992).

[32]S. O. Kucheyev, A. V. Hamza, J. H. Satcher Jr, and M. A. Worsley, “Depth-sensing indentation of low-density brittle nanoporous solids,” Acta Mater. **57**, 3472 (2009).

[33]K. Van Aeken, S. Mahieu, and D. Delpa, “The metal flux from a rotating cylindrical mangetron: a Monte Carlo simulation,” J. Phys. D: Appl. Phys. **41**, 205307 (2008).

[34]J. F. Ziegler and J. P. Biersack, SRIM-2013, Stopping power and range of ions in matter. 2013.

[35]W. M. Haynes, D. R. Lide, and T. J. Bruno, *CRC Handbook of Chemistry and Physics: A Ready-reference Book of Chemical and Physical Data*, (CRC Press, Boca Raton, FL, 2016).

[36]W. D. Westwood, *Sputter deposition* (AVS, New York, 2003).

[37]I. Petrov, I. Ivanov, V. Orlinov, and J. Kourtev, “Comparison of some basic plasma parameters and discharge characteristics of planar magnetron sputtering discharges in argon and neon,” Contrib. Plasma Phys. **2**, 223 (1990).

[38]J. A. Thornton, “Magnetron sputtering: Basic physics and application to cylindrical magnetrons,” J. Vac. Sci. Technol. **15**, 171 (1978).

[39]W. D. Westwood and S. Maniv, “The current-voltage characteristic of magnetron sputtering systems,” J. Appl. Phys. **54**, 6841 (1983).

[40]D. J. Economou, “Tailored ion energy distributions on plasma electrodes,” J. Vac. Sci. Technol. A **31**, 050823 (2013).

[41]R. A. Baragiola, E. V. Alonso, J. Ferron, and A. Oliva-Florio, "Ion-induced electron emission from clean metals," Surface Science **90**, 240 (1979).

[42]Y. Yoneda, "Anomalous surface reflection of x-rays," Phys. Rev. **131**, 2010 (1963).

[43]A.G. Dirks and H.J. Leamy, "Columnar microstructure in vapor-deposited thin films," Thin Solid Films **47**, 219 (1977).

[44]L. Abelmann and C. Lodder, "Oblique evaporation and surface diffusion," Thin Solid Films **305**, 1 (1997).

[45]A. Barranco, A. Borras, A.R. Gonzalez-Elipe, A. Palmero, "Perspectives on oblique angle deposition of thin films: From fundamentals to devices," Prog. Mater. Sci. **76**, 590153 (2016).

[46]J. M. Nieuwenhuizen and H. B. Haanstra, "Microfractography of thin films," Philips Techol. Rev. **27**, 87 (1966).

[47]R. N. Tait, T. Smy, and M. Brett, "Modeling and characterization of columnar growth in evaporated films," Thin Solid Films **226**, 196 (1993).

[48]K. Wittmaack, "Reliability of a popular simulation code for predicting sputtering yields of solids and ranges of low-energy ions," J. Appl. Phys. **96** (5), 2632 (2004).

TABLE I. Conditions of the four magnetron sputter deposition runs of the present study and film thicknesses for a substrate tilt angle (α) of 0°. Substrate temperature, a target-to-substrate distance (TSD), working gas (Ar or Ne) pressure, and the average discharge power for all four runs were fixed at 330 °C, 100 mm, 9 mTorr, and 300 W, respectively.

Deposition run label	Working gas	Power mode	Deposition time (h)	Target bias (V)	Film thickness at $\alpha = 0°$ (μm)
Ar-DC	Ar	DCMS	5	469	1.6
Ar-RF	Ar	RFMS	14	155	2.5
Ne-DC	Ne	DCMS	5	340	1.4
Ne-RF	Ne	RFMS	5	184	0.9

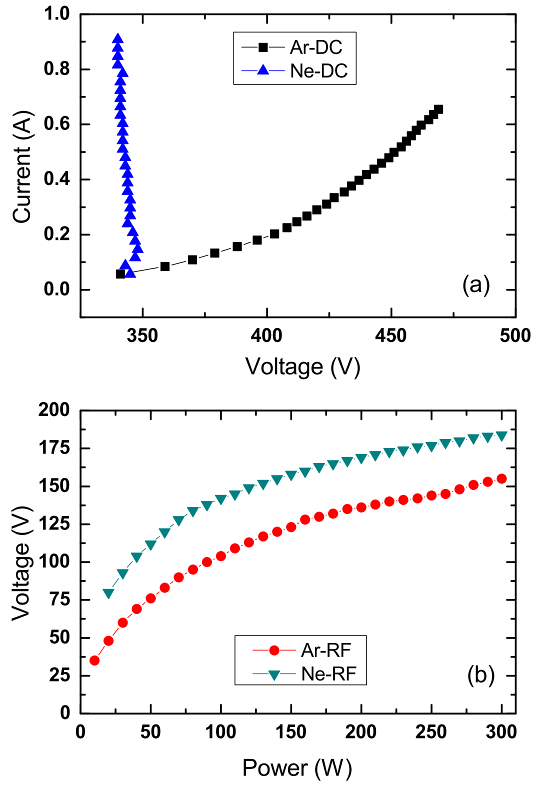

FIG. 1. (a) Current–voltage characteristics of the DCMS discharge and (b) target self-bias vs RF power dependencies for the RFMS discharge of B_4C at 9 mTorr of Ar or Ne, as indicated in the legends.

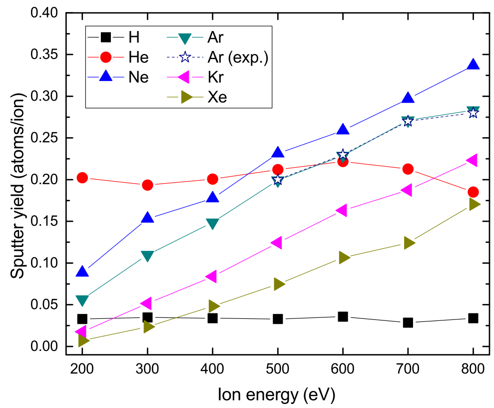

FIG. 2. Sputter yield of amorphous B_4C as a function of ion energy for different inert gases calculated with the TRIM code with input parameters adjusted so that the yield predicted for 500 eV Ar ions matched the experimental data point. Experimental data for sputtering with Ar ions is shown as open star symbols.

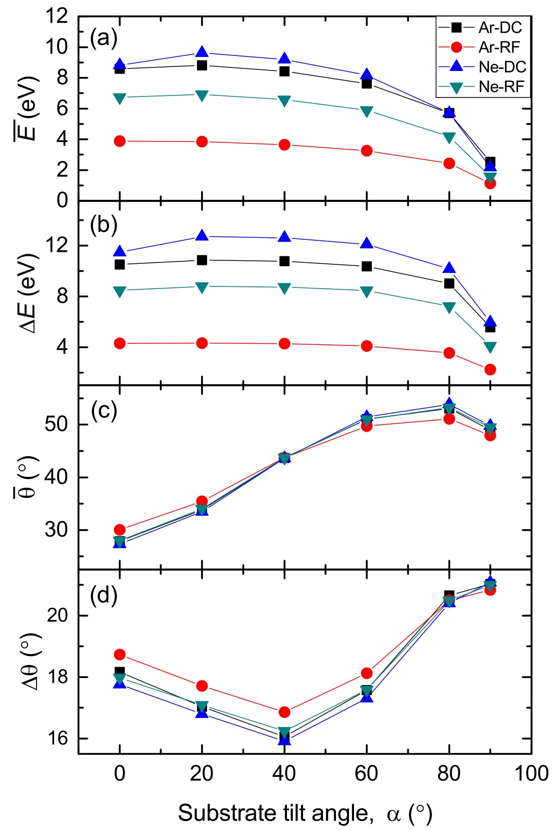

FIG. 3. Predictions of SiMTra/TRIM code simulations for substrate tilt dependencies of (a) average kinetic landing energy ($\overline{E}$) and (c) average incident angle ($\overline{\theta}$) as well as the standard deviation of distributions of (b) the landing energy (ΔE) and (d) incident angle ($\Delta\theta$) for depositing species (i.e., B and C atoms) during sputter deposition of B_4C under the conditions of the present study.

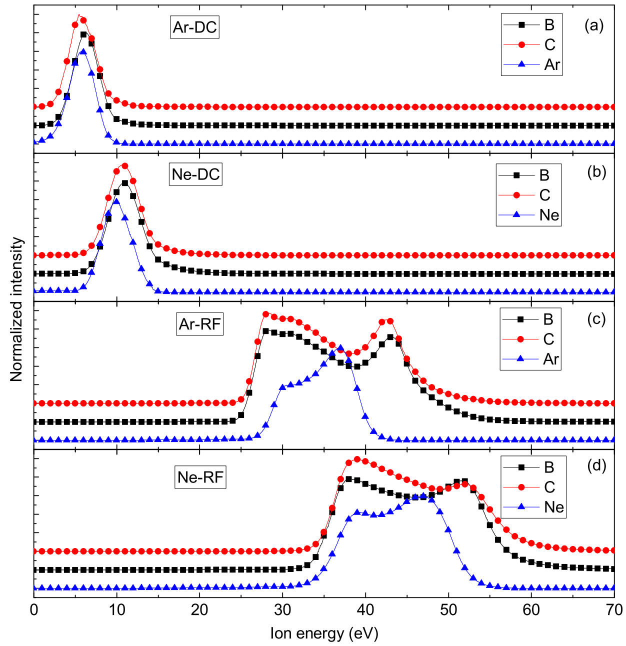

FIG. 4. Mass-resolved, time-integrated ion energy distributions measured with an electrostatic quadrupole probe for (a) Ar-DC, (b) Ne-DC, (c) Ar-RF, and (d) Ne-RF plasmas at the source axis, 100 mm away from the target surface at 9 mTorr of either Ar or Ne, as indicated in the legends. In each panel, the distributions are vertically offset, and only every 20th experimental point is depicted, for clarity. Each distribution was normalized to the intensity of its strongest peak.

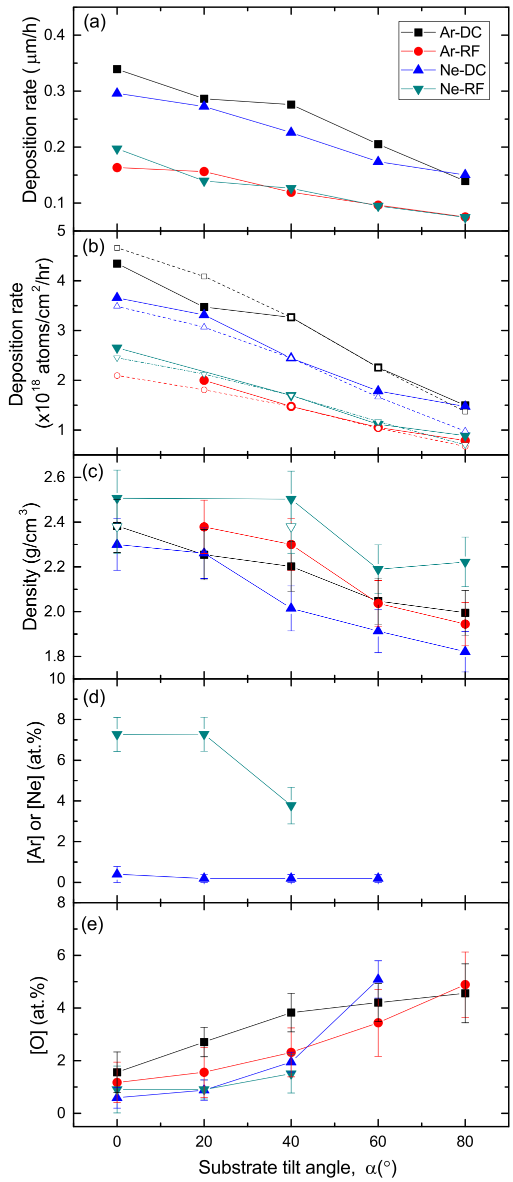

FIG. 5. Substrate tilt dependencies of the following film properties measured with the methods described in Sec. II B: (a) the physical thickness deposition rate (in μm/h), (b) the areal density deposition rate (in atoms/cm^2/h), (c) mass density, (d) working gas impurity content (Ar or Ne), and (e) oxygen impurity content in the four sets of B_4C films studied here. Missing data points in (d) indicate that the impurity concentration was below the detection limit of our RBS measurements. The legend in (a) relating the symbol type to the run label applies to all the panels. Open symbols in (b) show predictions of SiMTra/TRIM simulations scaled to experimental data at $\alpha = 40°$, and open down-triangles in (c) show mass density for Ne-RF films calculated after excluding Ne impurity atoms.

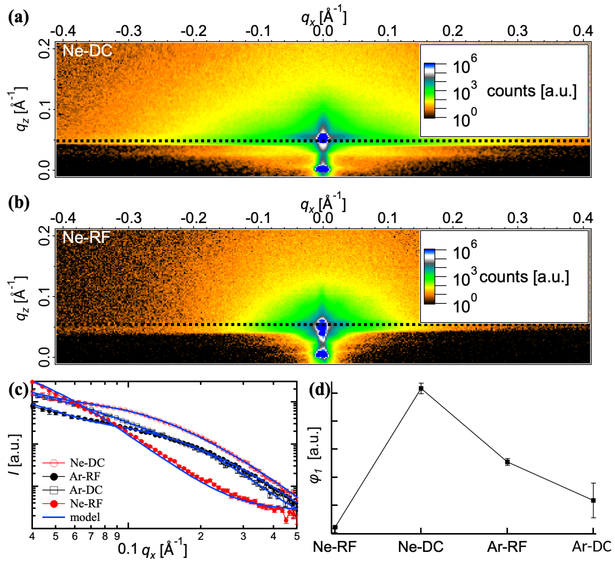

FIG. 6. Experimental GISAXS data obtained from ($\alpha = 0°$) B_4C films for (a) Ne-DC and (b) Ne-RF runs. It shows a clear decrease in scattered intensity for the Ne-RF film. The 1D in-plane scattering profiles are shown in (c), along with the model fits. The trend in the scaling parameter, ϕ_1, obtained from model fitting, with sputtering conditions is shown in (d).

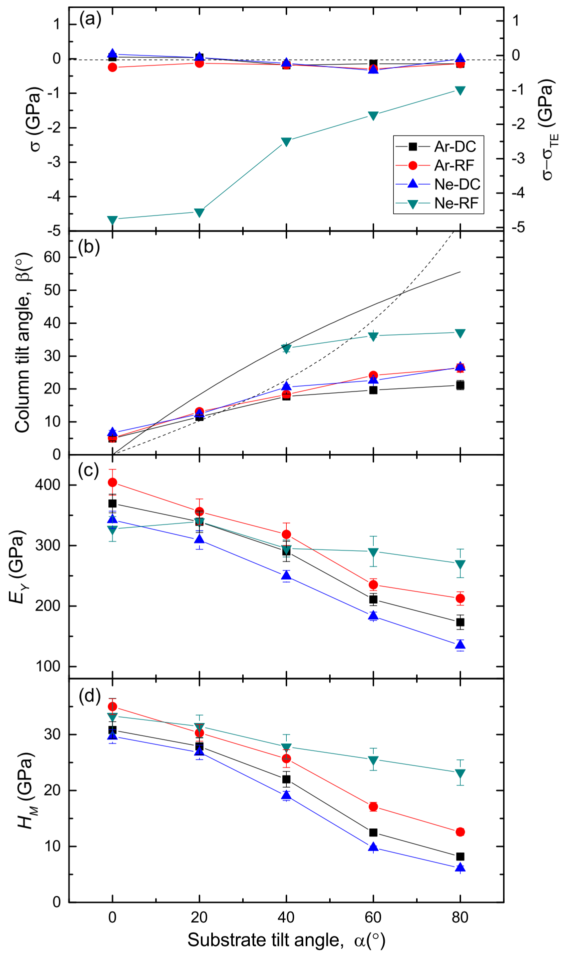

FIG. 7. Substrate tilt dependencies of the following film properties measured with the methods described in Sec. II B: (a) residual stress (σ, where σ_{TE} is the stress contribution due to the thermal expansion mismatch between the substrate and the film); (b) column tilt angle (β), with predictions of empirical cosine and tangent rules shown by solid and dashed lines, respectively; (c) Young's modulus (E_Y); and (d) Meyer's hardness (H_M) of B_4C films. The legend in (a) relating the symbol type to the run label applies to all the panels.

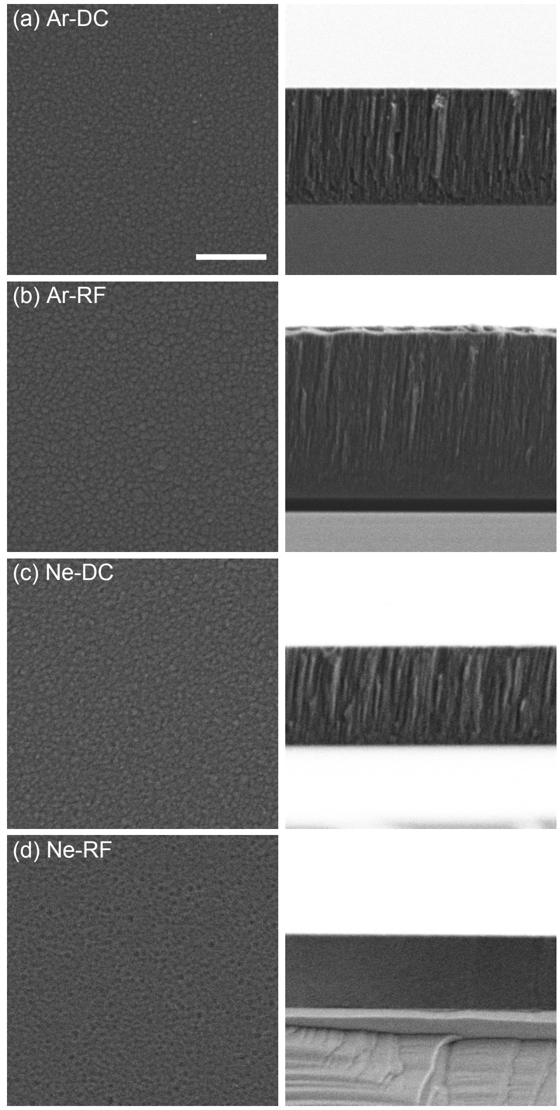

FIG. 8. Representative (left column) plan-view and (right column) fracture-cross-sectional SEM micrographs of films from deposition runs (a) Ar-DC, (b) Ar-RF, (c) Ne-DC, and (d) Ne-RF, as described in Table I for a substrate tilt angle of 0°. The scale bars in (a) is 1 μm, and it applies to all the panels.

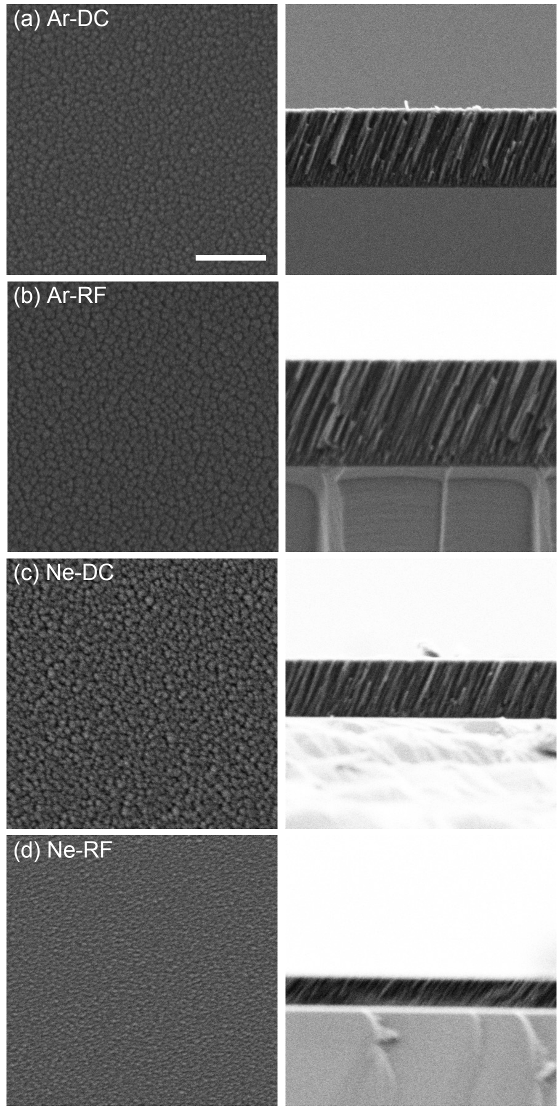

FIG. 9. Representative (left column) plan-view and (right column) fracture-cross-sectional SEM micrographs of films from deposition runs (a) Ar-DC, (b) Ar-RF, (c) Ne-DC, and (d) Ne-RF, as described in Table I for a substrate tilt angle of 60°. The scale bars in (a) is 1 μm, and it applies to all the panels.